ACS APPLIED MATERIALS & INTERFACES
Research Article
www.acsami.org

Influence of Sodium Halides (NaF, NaCl, NaBr, NaI) on the Photocatalytic Performance of Hydrothermally Synthesized Hematite Photoanodes

TsingHai Wang,[†] Mao-Chia Huang,[‡] Yi-Kong Hsieh,[†] Wen-Sheng Chang,[§] Jing-Chie Lin,[‡] Chih-Hao Lee,[⊥] and Chu-Fang Wang*[,†]

[†]Biomedical Engineering and Environment Sciences and [⊥]Department of Engineering and System Sciences, National Tsing Hua University, Hsinchu, Taiwan 30013

[‡]Institute of Materials Science and Engineering, National Central University, Jhongli City, Taiwan 32001

[§]Green Energy and Environment Research Laboratories, Industrial Technology Research Institute, Hsinchu, Taiwan 31040

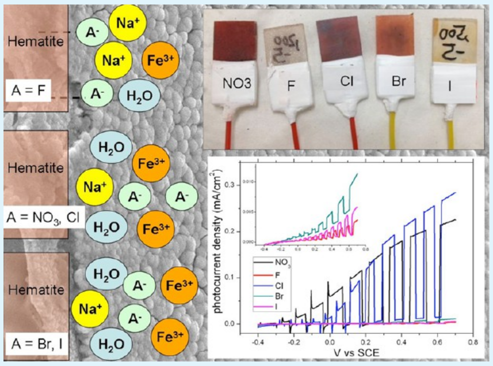

ABSTRACT: It has been suggested that a high concentration of Fe^{3+} in solution, a low pH, and noncomplexing ions of high ionic strength are all essential for developing a high-quality hematite array. Our curiosity was piqued regarding the role of the electrolyte ions in the hydrothermal synthesis of hematite photoanodes. In this study, we prepared hematite photoanodes hydrothermally from precursor solutions of 0.1 M $FeCl_3$ at pH 1.55 with a background electrolyte of 1.0 M sodium halide (NaF, NaCl, NaBr, or NaI). We compared the structures and properties of the as-obtained hematite photoanodes with those of the material prepared in 1.0 M $NaNO_3$, the most widely adopted electrolyte in previous studies. Among our studied systems, we found that the hematite photoanode prepared in NaCl solution was the only one possessing properties similar to those of the sample obtained from the $NaNO_3$ solution—most importantly in terms of photoelectrochemical performance (ca. 0.2 mA/cm^2 with +0.4 V vs SCE). The hematites obtained from the NaF, NaBr, and NaI solutions exhibited much lower (by approximately 2 orders of magnitude) photocurrent densities under the same conditions, possibly because of their relatively less ordered crystallinity and the absence of rodlike morphologies. Because the synthetic protocol was identical in each case, we believe that these two distinct features reflect the environments in which these hematite photoanodes were formed. Consistent with the latest studies reported in the literature of the X-ray photoelectron spectra of fast-frozen hematite colloids in aqueous solutions, it appears that the degree of surface ion loading at the electrolyte−hematite interface (Stern layer) is critical during the development of hematite photoanodes. We suspect that a lower ion surface loading benefits the hematite developing relatively higher-order and a rodlike texture, thereby improving the photoelectrochemical activity.

KEYWORDS: *hematite, photoanode, halide, electric double layer, photoelectrochemical cell*

■ INTRODUCTION

Slow progress in improving the efficiency of photoelectrochemical conversion of solar energy into chemical energy using semiconductor photocatalysts is hindering the wide-scale application of solar energy harvesting devices.[1−3] Among all of the available semiconductor photocatalysts (TiO_2, WO_3, α-Fe_2O_3), hematite (α-Fe_2O_3) is one of the most promising materials because of its abundance, environmental friendliness, and, most importantly, stability over a wide range of values of pH.[4] A band gap of 2.1 eV enables hematite to harvest approximately 38% of solar energy under air mass 1.5 global (AM 1.5 G) conditions.[5] Its photocatalytic efficiency remains, however, limited by several factors: rapid recombination of photogenerated charge carriers,[6] short hole diffusion lengths (2−4 nm),[7] low hole mobility (ca. 0.01 cm^2/(V s)),[8] slow rates of oxygen evolution,[9] and significant decreases in the absorption cross-section for wavelengths having energies close to the band gap.

Great improvements in photocatalytic efficiency have, however, been achieved through morphological nanoengineering and external doping strategies.[10] Hematite materials possessing cauliflowerlike structures[11] or mesoporous film structures[12,13] have been reported in the literature with high photoactivity. Recently, quasi-one-dimensional α-Fe_2O_3 structures, including wires, tubes, belts, and rods, have been synthesized.[14,15] Their high photocatalytic efficiencies are believed to be closely related to their large surface areas as well as their relatively few grain boundaries (potential scattering centers). Several versatile methods have been proposed for the preparation of these unique one-dimensional hematite structures, including template-directed synthesis,[16] sol−gel synthesis,[17] gas−solid reactions,[18] hydrothermal reactions,[19] anodic

Received: May 27, 2013
Accepted: July 18, 2013
Published: July 18, 2013

dx.doi.org/10.1021/am402024q | *ACS Appl. Mater. Interfaces* 2013, 5, 7937−7949

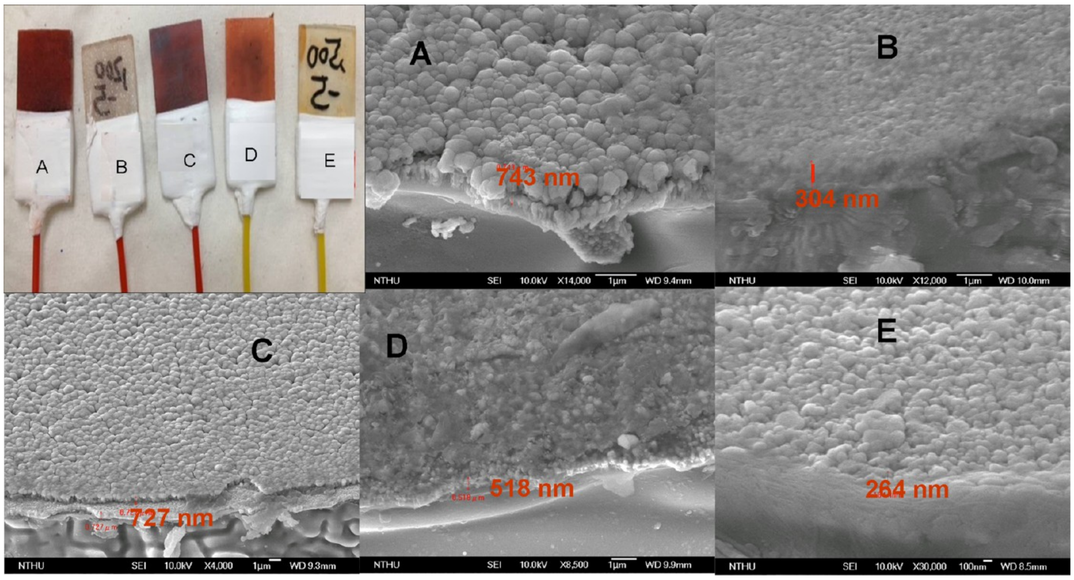

Figure 1. Photograph and corresponding SEM images of annealed hematite photoanodes obtained from high-ionic-strength electrolyte solutions containing 1.0 M (A) $NaNO_3$, (B) NaF, (C) NaCl, (D) NaBr, and (E) NaI. The reactive area of these hematite photoanodes was 1 cm^2.

oxidation,[20,21] thermal treatment on iron foil,[22] and template-accelerated hydrolysis.[23] Among these developed methods, the most widely applied and cost-effective strategies for preparing α-Fe_2O_3 are the forced hydrolyses of Fe(III) solutions through hydrothermal and solvothermal synthesis. It has been reported that a high concentration of the Fe(III) precursor, a low pH, and the presence of noncomplexing ions at high ionic strength are all essential for a hydrothermal synthesis to provide a high-quality hematite array.[24]

All previous successful hydrothermally syntheses of hematite photoanodes exhibiting high photoactivity have been performed using a high concentration of $NaNO_3$ (1.0 M) as the background electrolyte. This feature piqued our curiosity about the role of these electrolyte ions in the hydrothermal synthesis of hematite photoanodes. Accordingly, in this study we tested the hydrothermal synthesis of hematite photoanodes using precursor solutions of 0.1 M $FeCl_3$ with 1.0 M sodium halide (F^-, Cl^-, Br^-, I^-) as the background electrolyte at pH 1.55. After hydrothermal reactions at 120 °C for 4 h, we annealed the resulting hematite photoanodes at 500 °C for 30 min. We then compared the properties and photocatalytic performances of these materials with those of the sample prepared using 1.0 M $NaNO_3$ as the electrolyte under otherwise identical conditions. Among our prepared materials, we found that the hematite photoanode formed in the NaCl solution was the only one exhibiting properties similar to those of the hematite photoanode obtained from the $NaNO_3$ solution—most importantly, in terms of their photoelectrochemical performance (ca. 0.2 mA/cm^2 with +0.4 V vs SCE); the photocurrent densities of the other hematite photoanodes were approximately 2 orders of magnitude lower than those two. Because the synthetic protocol was the same in each case, the discrepancies presumably arose from the different interactions of the hematite with the various electrolyte anions at the hematite−electrolyte interfaces. Accordingly, we propose herein a possible mechanism for the phenomena occurring at the hematite−electrolyte interfaces during these hydrothermal syntheses.

■ EXPERIMENTAL SECTION

Fabrication of the hematite films was conducted in solutions of 0.1 M $FeCl_3$ (precursor) at low pH [pH 1.55, adjusted by adding conc HCl (36.5−38%)], where the electrolyte was 1.0 M $NaNO_3$, NaF, NaCl, NaBr, or NaI. Each solution was transferred to a Teflon-lined autoclave (capacity: 23 mL). A slide of FTO glass was loaded into the autoclave, and the Parr bomb reactor was then placed within an oven maintained at 120 °C for 4 h. The reactor was allowed to cool to ambient temperature, after which the sample was rinsed with deionized water and then blown dry with N_2. Samples were annealed at 500 °C for 30 min in air with a ramp rate of 10 °C/min. Herein, the nomenclature of the obtained hematite photoanodes follows the example of "$NaNO_3$-hematite" referring to the hematite photoanode synthesized from a solution containing 1.0 M $NaNO_3$. Each synthesis was repeated five times (i.e., five samples obtained from each electrolyte solution); the sample exhibiting a photocurrent closest to the average value [relative standard deviation (RSD): ca. 15%] was chosen for further analyses of morphology and crystallinity and through electrochemical impedance spectroscopy (EIS).

Sample morphologies were imaged using field-emission scanning electron microscopy (FE-SEM; JSM6700F, JEOL, Japan). Surface roughness was evaluated using atomic force microscopy (JPK NanoWizard AFM) probing five different spots (5 μm × 5 μm each) each sample. X-ray diffraction (XRD) patterns were measured on a D2 Phaser diffractometer (Bruker, Germany) using Cu Kα radiation (λ = 1.5418 Å); lattice refinement was performed using built-in Topas 4.2 software (Bruker, Germany). Linear sweep voltammetry was performed at a scan rate of 20 mV/s using a PGSTAT 30 AutoLab electrochemical workstation. Photoelectrochemical properties were investigated using a three-electrode configuration: a hematite film as the working photoelectrode, a saturated calomel electrode (SCE) as the reference electrode, and platinum foil as the counter electrode in 1 M NaOH. Sunlight was simulated using a 300-W xenon lamp (Spectra Physics) and an AM 1.5 G filter (Oriel); the light intensity was calibrated to 100 mW/cm^2. EIS was performed using a PGSTAT 30 AutoLab, with the data fitted to an equivalent circuit model using its built-in software (AutoLab). With the applied alternating current (AC) signal fixed at 10 mV, the frequency was scanned between 100 kHz and 0.1 Hz at potentials between −0.4 and +0.4 V (versus SCE) in the dark with an electrolyte of 1.0 M NaOH; Pt was the counter electrode. To develop Mott−Schottky plots of the as-obtained hematite photoanodes, the capacitance was extracted from the EIS spectra by using the condition $R_pC\omega^{max} = 1$, where C is the capacitance of the Helmholtz layer, R_p is the charge-transfer resistance ($R_p/2$ equals to the maximum value of

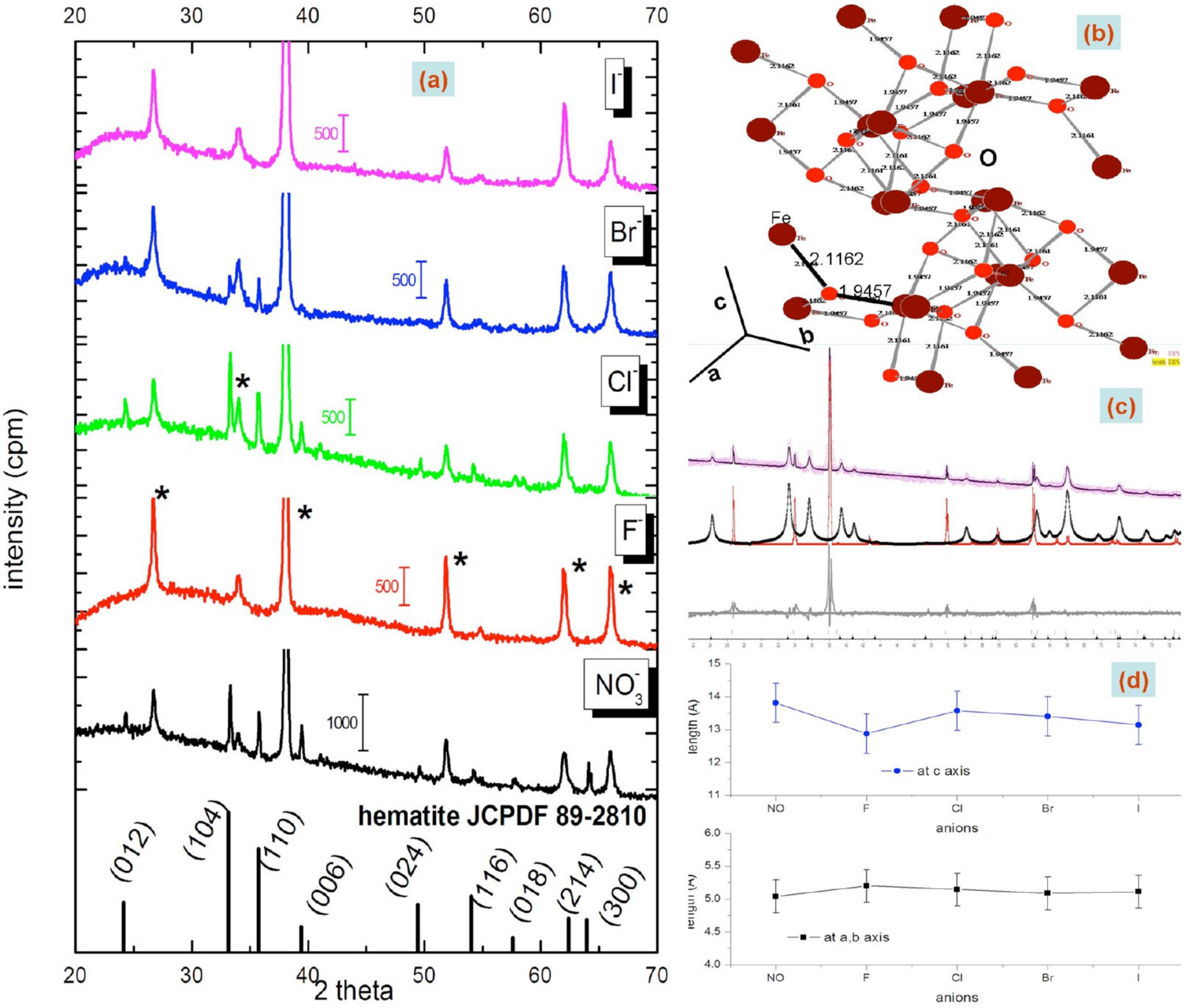

Figure 2. (a) XRD patterns of annealed hematite photoanodes obtained from high-ionic-strength electrolyte solutions containing 1.0 M $NaNO_3$, NaF, NaCl, NaBr, and NaI, respectively. (b) Structural model of hematite obtained from a Topas 4.2 software simulation based on rhombohedral symmetry (space group no. 167): $a = b = 5.038$ Å; $c = 13.772$ Å; $\alpha = \beta = 90°$; $\gamma = 120°$. (c) Illustration of the XRD lattice structure refinement (using Topas 4.2 software) of the hematite obtained from the NaBr solution. (d) Corresponding lattice variations along the *a*-/*b*-axes and *c*-axis.

imaginary impedance), and ω^{max} is the frequency corresponding to the maximum imaginary impedance of a semicircle.[33] To study the ion's surface loading on the hematite photoanode, the following operating conditions were applied for the laser ablation inductively coupled plasma mass spectrometry (LA-ICP-MS) system: LA was performed using a UP 213 laser ablation system (New Wave Research, USA) combined with a Nd:YAG laser (wavelength: 213 nm) and operated in Q-switched (pulsed) mode. The pulse length was 4 ns with a repetition rate of 10 Hz, a dwell time of 8 s, and an intersite pause of 1 s. During ablation, the laser beam (diameter 0.11 mm; defocused distance 1.5 mm) with fluence of 15−20 J/cm^2 was used to vaporize the elements within a selected area. At a scan rate of 0.1 mm/s and a frequency of 10 Hz, an area of approximately 3 mm ×3 mm was ablated and introduced into the ICP-MS system using argon as the carrier gas (1.0 L/min). Analyses of the elements Na, N, Fe, Cl, Br, and I were conducted using a quadrupole ICP mass spectrometer (Agilent 7500a, USA); the operating RF power was 1.5 kW, and the detector was operated in time-resolved analysis acquisition mode; the plasma gas flow rate and auxiliary gas flow rate were 15 and 2.0 L/min, respectively.

■ RESULTS AND DISCUSSION

Morphological Properties. The upper-left panel in Figure 1 presents a photograph of the annealed hematite photoanodes that we obtained from high-ionic-strength electrolyte solutions containing 1.0 M $NaNO_3$, NaF, NaCl, NaBr, and NaI, respectively. The NaF- and NaI-hematites were rather transparent; the NaBr-hematite was light brown, while the $NaNO_3$- and NaCl-hematites were deep red. These different colors and darknesses appear to have arisen simply from the different thicknesses of these as-obtained hematite photoanodes. SEM cross-sectional imaging revealed that the $NaNO_3$- and NaCl-hematites possessed relatively rodlike structures having thicknesses of approximately 700 nm. In contrast, those grown in the NaF, NaBr, and NaI solutions had rodlike appearances on their surfaces and densely packed films in their interiors; their thicknesses, in a range from 200 to 500 nm, were responsible for their relatively transparency. It has been reported that the pH, reaction time, and concentration of the precursor all significantly affect the growth of hematite arrays.[24] An environment with a lower pH and an elongated reaction time will both favor the hematite developing toward longer rods and wires.[25] In our case, however, all of the synthetic conditions were identical, meaning that the distinct morphologies and thicknesses presumably reflected the history during the growth of these hematite photoanodes; that is, the structures reflected the chemical environments induced by the different electrolyte ions.

XRD Analysis. After annealing at 500 °C, the as-obtained hematite photoanodes had the form of α-Fe_2O_3 (JCPDS card number 89−2810), as confirmed from the XRD patterns in Figure 2. We observed no other crystalline phases, except that of the FTO substrate. The patterns of the $NaNO_3$- and NaCl-hematites featured two strong (104) and (110) reflections along with several minor reflections corresponding to the (012), (006), (024), (116), (018), and (300) planes. The XRD pattern of the hematite obtained from the NaBr solution was similar to those of the samples grown from the $NaNO_3$ and NaCl solutions, but its signal intensity was much lower. In contrast, the characteristic reflections of the NaF- and NaI-hematites were very difficult to detect; because their signals were low and blurry, we had to seek for help from the built-in Topas 4.2 software to extract them from of background intensity. Figure 2c presents an example of the extracted XRD reflections for NaI-hematite. Through successive treatment, including baseline adjustment, lattice refinement of FTO, peak shift correction, and intensity adjustment (the intensity from FTO has been square rooted while that of hematite left unchanged), we isolated the reflections of NaI-hematite as indicated by the black line. We applied the same protocol for further lattice refinement of all of the other hematite samples (see below). Given that the reflection intensity is positively proportional to the crystallinity, the clearer XRD patterns of the $NaNO_3$- and NaCl-hematites suggested that their structures were relatively highly ordered, consistent with the FE-SEM images in Figure 1. Conversely, the blurry XRD patterns reflect the character of less-ordered hematite films grown in the NaF, NaBr, and NaI solutions. Notably, a hump appeared at a value of 2θ between 20 and 30° in the cases of the NaF-, NaBr-, and NaI-hematites. We might suspect that annealing at 500 °C for 30 min was not sufficient to completely convert these samples into the pure hematite phase. Nevertheless, because we confidently isolated hematite reflections from the observed XRD patterns (with the assistance of Topas 4.2 software) and because additional annealing at higher temperature or elongated time would have bent our FTO substrates, we did not conduct any further annealing but believe they these materials featured pure hematite phases. Accordingly, we interpret the presence of the hump as evidence of relatively poor crystallinity. In other words, the environments in the NaF, NaBr, and NaI solutions were not favorable for developing high-quality hematites.

We further conducted lattice refinement with the assistance of Topas 4.2 software to evaluate the influence of the different electrolyte anions on the growth of hematite (using the same protocol mentioned above). Figure 2d reveals that the different electrolyte anions had no effect on the hematite growing toward the *a*- and *b*-axes. On the other hand, the presence of NO_3^- and Cl^- anions did enhance the hematite developing along the *c*-axis. We observed smaller *c*-axis parameters for the hematite samples grown in the NaF, NaBr, and NaI solutions. On the basis of the results of lattice refinement, growth along the *c*-axis favors a hematite sample developing a rod-like appearance. In addition, the SEM images in Figure 1 provided further evidence for the different electrolyte anions affecting the morphologies of these hematite photoanodes; from the point of view of lattice structure, however, they led to lattice variations only along the *c*-axis.

Morphological control is a very important and interesting aspect of the field of nanoengineering. It strongly relies on knowledge of the structure of the solid−solution interface. Several recent literature reports of the synthesis of hematite nanoparticles (NPs) with controllable morphology suggest that the presence of structure-directing agents plays a greater role than that of the electrolyte anions. For example, the presence of oleic acid assists the growth of hematite NPs into a narrow size distribution;[26] the degree of chelation between 5-sulfosalicylic acid and Fe(III) is an important factor controlling the morphology of hematite nanocrystals;[27] hematite particles having a platelike morphology can be obtained by adjusting the water/ethanol ratio during the hydrothermal reaction;[28] and cubic hematite microparticles can be synthesized using a mixture of glycine and ferric chloride in a simple one-step hydrothermal reaction.[29] In our case, however, we did not add any relevant structure-directing agents; therefore, the observed distinct surface morphologies must have arisen from the hematite samples developing in different environments.

Photoelectrochemical Behavior. Figure 3a displays the photoelectrochemical performance of the hematite photoanodes that we had grown in the various electrolyte solutions. Under a bias potential of +0.4 V (vs SEC), the $NaNO_3$- and NaCl-hematites exhibited photocurrent densities close to 0.2 mA/cm^2.

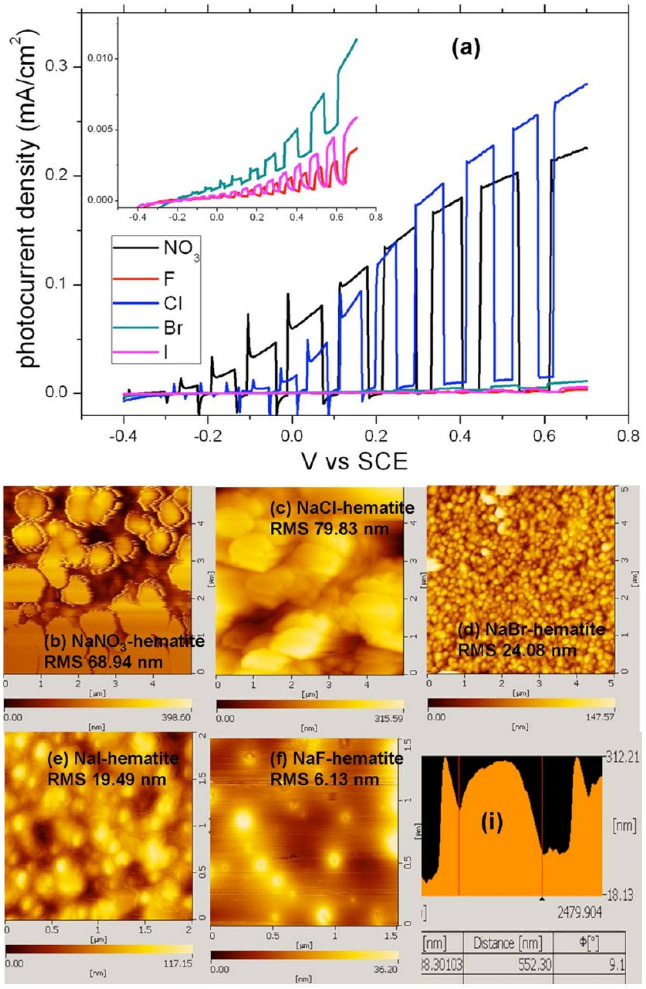

Figure 3. (a) Photoelectrochemical performance of annealed hematite photoanodes obtained from high-ionic-strength electrolyte solutions containing 1.0 M $NaNO_3$, NaF, NaCl, NaBr, and NaI, respectively. Representative surface roughness of (b) $NaNO_3$-, (c) NaCl-, (d) NaBr-, (e) NaI-, (f) NaI-hematite photoanode collected from AFM analysis. (i) Representative surface roughness profile analysis of NaCl-hematite photoanode.

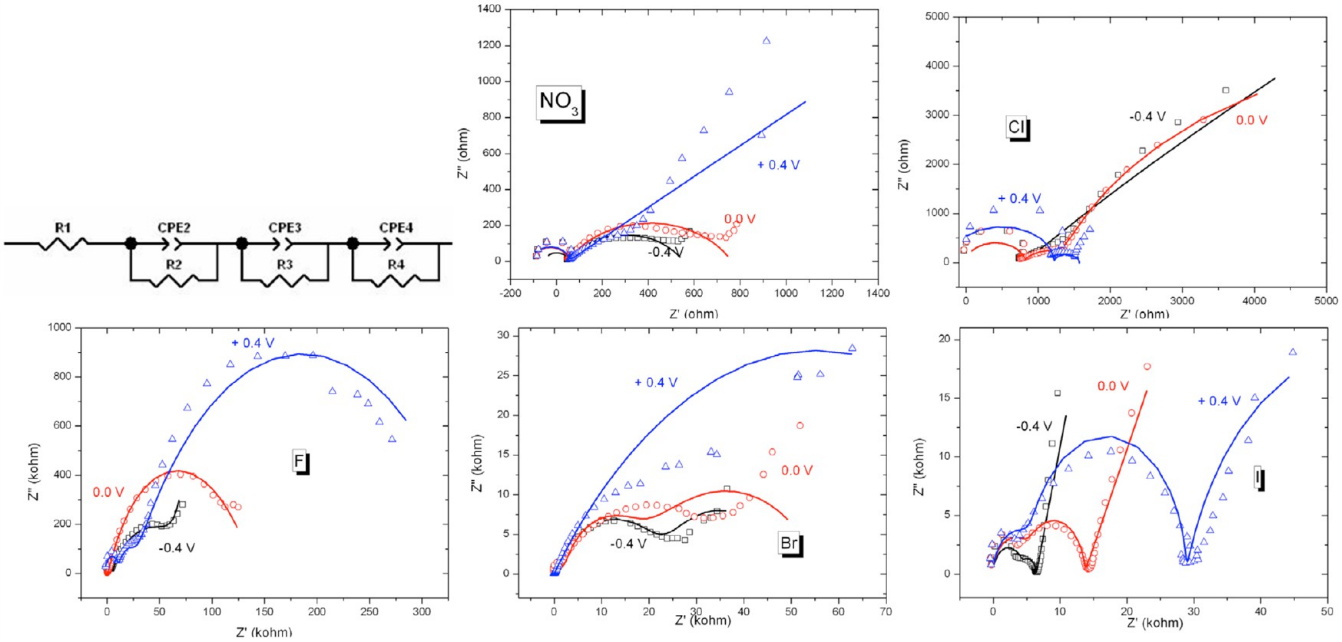

Figure 4. Electronic impedance spectra of hematite photoanodes obtained from various electrolyte solutions. All spectra were collected in the dark (without illumination) under applied external biases of −0.4 (black), 0.0 (red), and +0.4 V (blue) vs SCE.

In contrast, the photocurrent densities of the hematites obtained from the NaBr, NaI, and NaF solutions were all less than 0.005 mA/cm^2 under the same conditions—approximately 2 orders of magnitude lower than those obtained from the NaNO$_3$ and NaCl solutions. The observed photocurrents followed the order NaCl ~ NaNO$_3$ ≫ NaBr > NaI > NaF. The observed photocurrents of the NaBr-, NaI-, and NaF-hematites, although very small, together with the fact that we observed no photocurrent for the as-prepared hematite photoanodes in the absence of annealing, is further evidence of their intrinsic hematite properties. For an indirect band gap semiconductor, such as hematite, the transition of an electron from the valence to conduction band is phonon-assisted because a change in both energy and momentum is involved.[30] Given the low electrical conductivity of pure hematite, nanoengineering is widely adopted to increase the diffusion length of holes near the electrolyte interface. The [110] direction provides an excellent path for diffusion of electrons because of the strong anisotropic conductivity of hematite;[25] conduction is 4 orders of magnitude lower along the [001] direction than it is in the perpendicular (100) plane, which contains the [110] direction.[31] In addition, conduction in rod-structured hematite is much higher than that in any other morphology because of lower number of grain boundaries (possible recombination centers) and orientation perpendicular to the substrate.[32] Because we sintered all of our present samples at 500 °C, a temperature that is not sufficiently high for Sn diffusion,[12] we can reasonably rule out the possibility of introduction of an extrinsic dopant. Accordingly, the observed high photocurrent densities of the NaCl- and NaNO$_3$-hematites presumably resulted from better development in the (110) plane, as suggested in the XRD patterns (Figure 2). The same argument holds for the observed photocurrent of the NaBr-hematite being greater than those obtained from the NaI and NaF solutions. The very small saturation photocurrents (ca. 10 μA/cm^2) exhibited by the NaBr-, NaI-, and NaF-hematites suggest, however, that poor development of the (110) plane alone is not sufficient to explain their poor photoactivity. Their cross-sectional images in Figure 1 suggest another possible factor: a much greater number of recombination centers existing along their dense interiors.

We further collected their surface roughness of these samples to evaluate the "actual" sample area (different from the projected area during photocurrent measurements) by using AFM with tapping mode (Figure 3b–i). On the basis of analyses of five different spots (5 μm × 5 μm each), corresponded average surface roughness (in terms of root-mean-square, RMS) follows the order of NaCl- (79.83 nm) ~ NaNO$_3$- (68.94 nm) > NaBr- (24.08 nm) ~ NaI- (19.49 nm) > NaF-hematite (6.13 nm). This order is consistent with the photocurrent performance (Figure 3a), suggesting a positive correlation between surface roughness and photocatalytic performance. In addition, higher surface roughness reflects the rodlike surface morphology of NaCl- and NaNO$_3$-hematite samples, while the lowest surface roughness of NaF-hematite photoanode reveals its filmlike surface morphology. Higher surface roughness exposes more surface area, which benefits more charge transfer taking place at hematite/electrolyte interface. On the basis of AFM analysis results, it is clear that higher surface roughness accounts for certain degree of better photocatalytic performance. However, given that the spread of surface roughness among these samples is only about 1 order of magnitude, which is 1 order of magnitude lower than observed photocatalytic performance. As a result, surface roughness would not be a major factor explaining distinct photocatalytic performance of these samples.

Electrochemical Impedance Spectroscopy. To better understand the roles of these electrolytes on the electronic properties of the hematite photoanodes, we recorded electrochemical impedance spectra in the dark and fitted them with the equivalent circuit R1[R2Q2][R3Q3][R4Q4], where R refers to a resistor while Q represents a constant phase element (CPE). We selected a CPE, rather than a capacitor, to account for the imperfect capacitor induced by the existence of an electrical double layer at each interface. The admittance (reciprocal of impedance) of CPE is defined as

$$Y_{\mathrm{CPE}} = Q_0(\omega i)^n$$

where a value of n of 1 represents an ideal capacitor and a value of 0 describes a pure resistor. Adopted equivalent circuits, also known as brick models, are widely applied in the fitting of EIS spectra of solid oxide fuel cells; they describe the carrier transport (proton transport) inside the grain and grain boundary.[34] Here, we assigned R1 as the resistance at the FTO−wire ohmic contact, R2 for the resistance at the FTO−hematite interface, R3 for the resistance inside hematite, and R4 for the resistance at the hematite−electrolyte interface.

In Figure 4, the shape of each EIS spectra depended on the applied bias potential and the environment in which these hematite photoanodes had been developed. Notably, fitting the low frequency region was quite difficult. Taking the $NaNO_3$-hematite as an example, the low frequency tail measured under a bias potential of +0.4 V might have arisen from large resistance at the hematite−electrolyte interface, electrode polarization, or carrier diffusion. In the latter case, a 45° straight tail would appear and a Warburg element could be adopted to account for such semi-infinite linear diffusion. Such assignment requires, however, precise acquisition of more reliable data because these low-frequency data would be rather erratic if no appropriate shielding were applied. For comparison, we preferred to assign this low-frequency region as a resistor and a CPE in parallel and adopted the brick model to interpret all acquired EIS spectra. Table 1 lists all of the fitting data; Figure 5 presents plots of the determined resistances and capacitances.

For the $NaNO_3$-hematite, a small semicircle appeared at the negative impedance region under all applied bias potentials (−0.4, 0.0, or +0.4 V vs SCE); its cause remains unclear, but this feature led to the generation of negative values of R1 from all fittings. A reasonable interpretation would be that the ohmic contact between the wire and FTO was rather small. Under applied biases of −0.4 and 0.0 V, it would be difficult to isolate the individual contributions R2, R3, and R4 because they were coupled together and did not feature any clear semicircles. This behavior mirrors the comparable values of R2, R3, and R4 that we observed from the fitting results. We rationalize the larger impedance in the case of a bias of 0.0 V (greater x intercept) than that under a bias of −0.4 V to the occurrence of charge carrier accumulation. As indicated in Table 1, the value of Q increased upon decreasing the value of n when we applied a more-positive bias; this behavior implies that the CPE gradually changed from a capacitor-like element into a resistor-like one. Together with an increase in capacitance, we suspect that increasing resistance resulted from accumulation of charge carriers. That is, the applied external bias potential mobilized these charge carriers so that they could transverse readily within the hematite grain. These mobile charge carriers would then accumulate at the regions where the resistances were rather large (e.g., grain boundaries) and, thus, develop an electrical double layer. In Figure 5 and Table 1, we note the charge carrier accumulation occurred mainly in the interior of the hematite and at the hematite−electrolyte interface, as evidenced by increases in the values of Q3 and Q4 by one and 2 orders of magnitude, respectively. Although the value of Q2 also increased by 2 orders of magnitude, we suspect that the degree of charge carrier accumulation at the FTO−hematite interface would be negligible when the value of n was 1 because of the low value of Q2 (4.07×10^{-11} F at −0.4 V).

On the other hand, when we applied a bias of +0.4 V, a clear rising tail appeared but it did not increase any resistance

Table 1. Fitting Results Based on the Equivalent Circuit R1(R2Q2)(R3Q3)(R4Q4)

anion	applied bias (V vs SCE)	photocurrent (A)	R1 (Ω)	R2 (Ω)	Q2 (F)	n	R3 (Ω)	Q3 (F)	n	R4 (Ω)	Q4 (F)	n
NO_3^-	−0.4	-1.63×10^{-5}	−23.4	86	4.07×10^{-11}	1	506	2.20×10^{-9}	1	96	3.99×10^{-9}	1
	0.0	6.92×10^{-5}	−84.7	39.4	6.99×10^{-9}	1	114	2.54×10^{-8}	0.671	71.5	1.38×10^{-7}	0.684
	+0.4	1.80×10^{-4}	−37	27	1.84×10^{-9}	1	288	3.17×10^{-8}	0.459	80.9	5.48×10^{-7}	0.378
F^-	−0.4	-4.37×10^{-6}	−22	1.28×10^4	4.84×10^{-11}	1	3.25×10^5	7.32×10^{-11}	0.641	1.33×10^4	1.64×10^{-9}	0.959
	0.0	3.12×10^{-7}	−430	5.7×10^3	1.55×10^{-10}	1	1.13×10^5	3.30×10^{-10}	0.656	2.56×10^4	1.02×10^{-7}	0.892
	+0.4	1.62×10^{-6}	−231	4.15×10^3	1.55×10^{-10}	1	6.69×10^4	5.84×10^{-10}	0.592	1.12×10^4	1.66×10^{-6}	0.874
Cl^-	−0.4	-1.18×10^{-6}	−17	79	5.99×10^{-10}	1	1061	6.35×10^{-10}	1	3358	2.12×10^{-8}	0.980
	0.0	2.15×10^{-5}	−17	80	6.02×10^{-10}	1	765	2.19×10^{-8}	0.819	2504	1.02×10^{-7}	0.884
	+0.4	2.10×10^{-4}	−19	89	3.94×10^{-10}	1	563	1.35×10^{-7}	0.557	1048	1.07×10^{-6}	0.256
Br^-	−0.4	-3.54×10^{-6}	−22	892	1.03×10^{-10}	1	2.58×10^4	5.03×10^{-10}	1	2.20×10^4	1.75×10^{-9}	0.679
	0.0	9.56×10^{-7}	−45	988	4.49×10^{-10}	1	3.93×10^4	2.57×10^{-9}	0.683	1.56×10^4	1.06×10^{-9}	0.603
	+0.4	4.92×10^{-6}	−34	975	3.94×10^{-10}	1	4.35×10^3	6.35×10^{-9}	0.609	1.07×10^4	2.13×10^{-8}	0.576
I^-	−0.4	-4.42×10^{-7}	−13	4.31×10^3	1.79×10^{-10}	1	2.10×10^4	6.81×10^{-10}	0.976	3.99×10^4	1.75×10^{-9}	0.879
	0.0	3.53×10^{-7}	−13	5.13×10^3	1.95×10^{-10}	1	8.46×10^3	1.95×10^{-9}	0.883	1.56×10^4	8.06×10^{-9}	0.703
	+0.4	2.28×10^{-6}	−14	2.34×10^3	1.23×10^{-9}	1	5.42×10^3	8.02×10^{-9}	0.751	1.07×10^4	9.13×10^{-8}	0.676

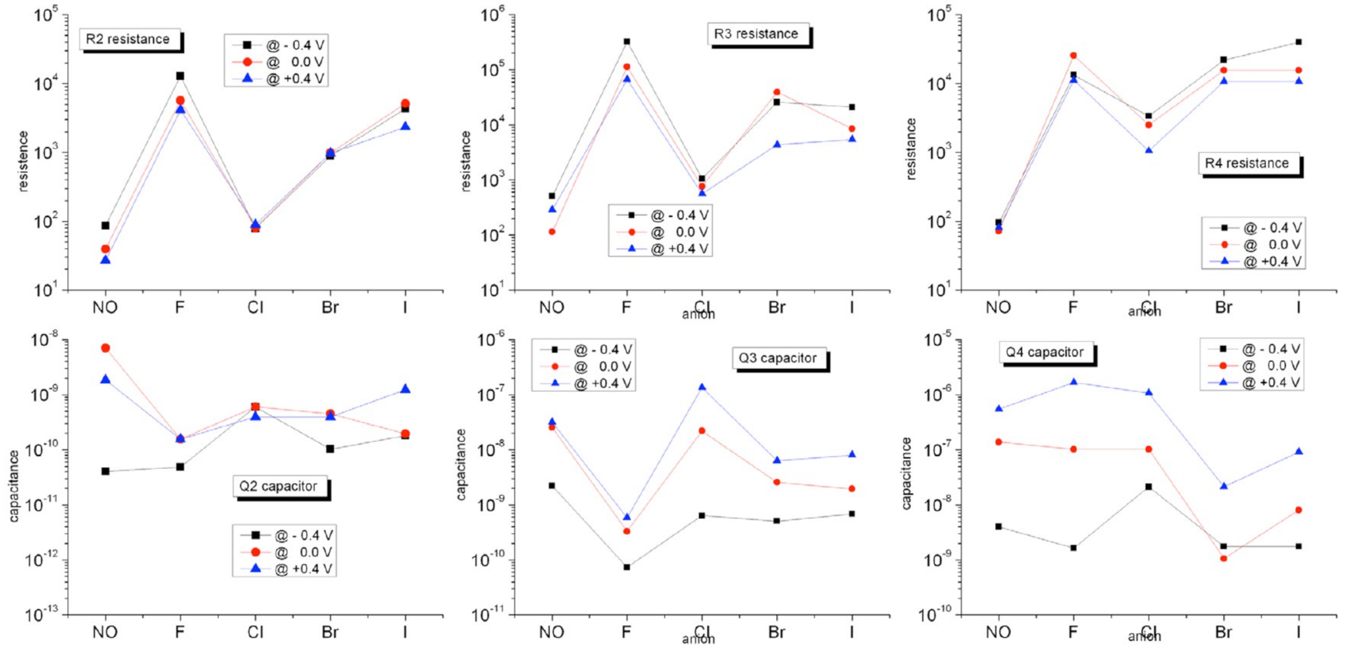

Figure 5. Variations in obtained resistance (R) and capacitance (Q) at the FTO−hematite interface (R2, Q2), within the hematite (R3, Q3), and at the hematite−electrolyte interface (R4, Q4) for hematite photoanodes obtained from various electrolyte solutions.

significantly; instead, it increased the level of capacitance. The values of both Q3 and Q4 increased slightly along upon increasing the external bias from 0.0 to +0.4 V. We would expect a higher degree of charge carrier accumulation upon decreasing the value of *n* from approximately 0.6 to approximately 0.4. Because all our EIS spectra were collected in the dark, the capacitance behavior (charge carrier accumulation) was simply a result of the low conductivity of the hematite. Meanwhile, the level of capacitivity can reflect the population of accumulated effective charge carriers. On the basis of our EIS fitting results, the applied external bias potential has the ability to mobilize charge carriers, which will accumulate at grain boundaries as well as at the hematite−electrolyte interface.

Next, we examined the EIS spectra and their corresponding fitting data for NaCl-hematite. Similar to the behavior of the $NaNO_3$-hematite, we observed some negative impedances, suggesting again that the ohmic contact between the wire and FTO was negligible. On the other hand, the impedances of the NaCl-hematite were somehow higher (by approximately 5-fold) than those of the $NaNO_3$-hematite. Its imaginary impedances were also much higher and, thus, the intermediate and low frequency tails appeared to be stretching upright. This interesting feature clearly reflects the higher degree of charge carrier accumulation, as evidenced by the values of the capacitances Q3 and Q4 being higher than those of the $NaNO_3$-hematite. In addition, the resistance at the hematite−electrolyte interface increased considerably, by approximately 2−3 orders of magnitude. Given the comparable photoactivities of the $NaNO_3$- and NaCl-hematites, we suspected that the higher values of R3 and R4 in the NaCl-hematite might reflect a higher value of capacitance. That is, the mobility of those charge carriers was slightly restricted as a result of repulsion among the charge carriers where they had built up. Although we have not conducted any measurements to prove it, such a decrease in mobility somehow increased the resistance within the hematite and at the hematite−electrolyte interface. Meanwhile, similar to the behavior of the $NaNO_3$-hematite, increasing the applied bias mainly increased the values of Q3 and Q4 upon decreasing their values of *n*. Based upon our fitting results, we conclude that highly photoactive hematite photoanodes will often exhibit relatively low resistance within the hematite and a high degree of capacitance at the hematite−electrolyte interface. In addition, the capacitance in the NaCl-hematite was higher than that in the $NaNO_3$-hematite, suggesting that more charge carriers were involved, thereby leading to a slightly higher photocurrent.

For NaBr-hematite, the shapes of the signals in the EIS spectra resemble those observed for $NaNO_3$-hematite, but both the real and imaginary impedances were approximately 2 orders of magnitude larger. In this case, two clear depressed semicircles appeared. A depressed semicircle can arise as a consequence of a linear combination of a series of resistors or when the contribution from the capacitor becomes weaker. Either way, the appearance of a clear semicircle implies that the resistance was significant, even though its value was not particularly large.[34] Upon increasing the applied bias, the low frequency part of the spectrum stretched toward the region of much larger impedance. As in the spectra of the $NaNO_3$- and NaCl-hematites, this feature suggests that charge diffusion occurred at the hematite−electrolyte interface. Table 1 reveals that the resistance at the wire−FTO interface was negligible. The resistance at the FTO−hematite interface was somehow 1 order of magnitude larger than those in the $NaNO_3$- and NaCl-hematites, but the values of both R2 and Q2 were unaffected, upon increasing the applied bias voltage. The values of R3 were approximately 2 orders of magnitude larger than those of the $NaNO_3$- and NaCl-hematites, whereas the values of Q3 were approximately 1 order of magnitude lower. These features explain the large impedance span—over tens of kilo-ohms—in the EIS spectra. Importantly, a 1 or 2 orders of magnitude increase in the value of R4 together with a 2 orders of magnitude decrease in the value of Q4 value suggests a much larger resistance at the hematite−electrolyte interface. Such a large resistance would definitely decrease the mobility of the charge carriers. This feature significantly decreased the photoactivity of the NaBr-hematite and, thus, its

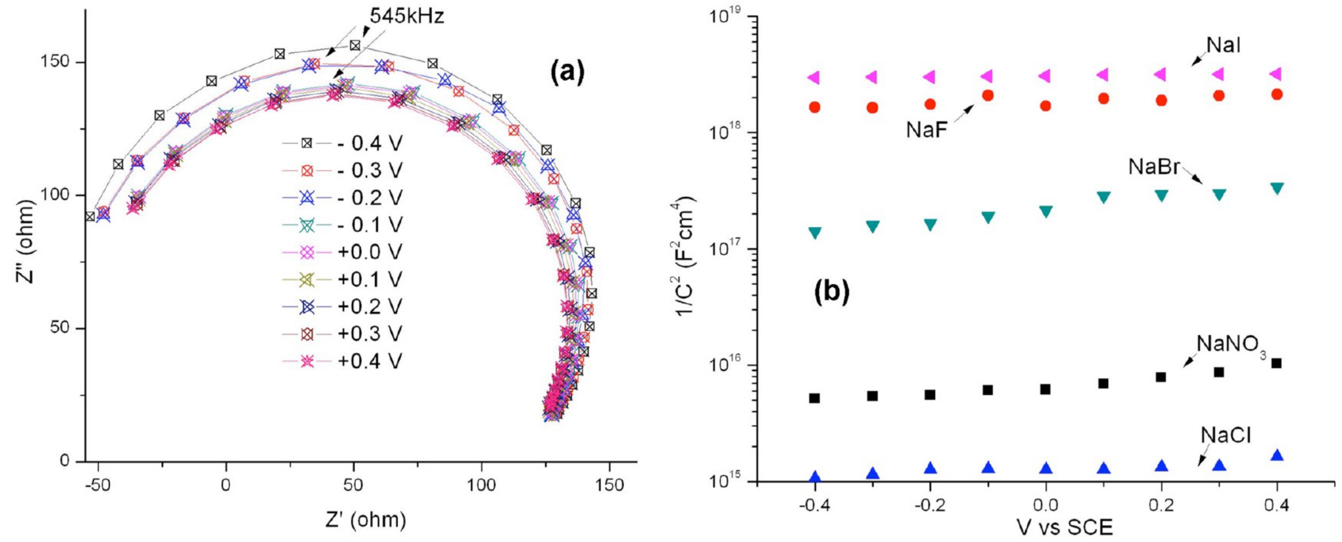

Figure 6. (a) Representative EIS spectra recorded between 100 MHz and 10 kHz and individual imaginary impedance maximum and its corresponding frequency are indicated. (b) Mott−Schottky plots of hematite photoanodes obtained from various electrolyte solutions.

photocurrent was approximately 1 order of magnitude lower than those of the $NaNO_3$- and NaCl-hematites.

The EIS spectra of the NaI-hematite features three clear semicircles, the impedances of which increased upon increasing the bias. This feature reveals unambiguously that the resistances at the FTO−hematite interface, within the hematite, and at the hematite−electrolyte interface were all significant. Accordingly, the conductivity was low in these three regions, explaining the observed low photoactivity of the NaI-hematite. Our fitting of the three semicircles implied that the resistances were approximately 3 orders of magnitude greater than those of the $NaNO_3$-hemetite. On the other hand, the values of both Q3 and Q4 were much lower than those of the $NaNO_3$-hematite, suggesting that a much lower level of charge carrier accumulation occurred within the hematite and at the hematite−electrolyte interface. Together, these features led to the NaI-hematite exhibiting a low photocurrent density (ca. 2.28 μA/cm^2 under an applied voltage of +0.4 V vs SCE). The NaF-hematite exhibited the largest impedance among all of these tested hematite photoanodes; similar to the fitting results for the NaI-hematite, it exhibited much larger resistances within the hematite and at the hematite−electrolyte interface. In particular, the resistance within the hematite was 1 order of magnitude larger than that in the NaI-hematite. Meanwhile, the capacitance of the NaF-hematite was quite low. Together, these features were responsible for this material exhibiting the lowest photoactivity performance.

Our EIS studies revealed that a high-performance hematite photoanode is often accompanied by a low resistance together with a high capacitance. The low resistance allows electrons to diffuse away from the particle to the back contact (the FTO electrode),[32] whereas the high capacitance indicates that more charge carriers participate in this reaction. Here, we extracted the capacitance of our hematite photoanodes from their EIS spectra though the use of a simple equivalent circuit, $R_s(C - R_p)$. Figure 6 displays the determined Mott−Schottky plots. On the basis of eq 1, the charge carrier density (N_A) can be derived from slope of $1/C^2$ against V, where e is the charge of an electron (1.6×10^{-19} C), ε_0 is the permittivity of free space (8.85×10^{-12} F/m), and ε is the relative dielectric constant of hematite (80).

$$\frac{1}{C^2} = \frac{2}{e\varepsilon\varepsilon_0 N_A}(E) \tag{1}$$

Table 2 summarizes the as-determined values of R^2, the slopes, and the charge carrier densities of the hematite photoanodes we obtained from the various electrolyte solutions. Because the strategy used to extract the slope strongly affects the determined value of the slope, we adopted a simple linear regression to determine the corresponding slope. With the exception of the NaI-hematite, the values of R^2 of all of the hematite photoanodes were far from unity, reflecting the fact that the capacitance did not respond linearly to the rising potential. Positive slopes in Mott−Schottky plots indicate n-type doping properties for metal oxide semiconductors while a p-type Mg-doped hematite synthesized recently through atomic layer deposition exhibited a very low turn-on voltage as a result of its internal p−n junction.[35] The charge carrier densities extracted from the slopes were in the region between 4×10^8 and 4×10^{11} 1/cm^3. Consistent with the order of the photocurrents, the $NaNO_3$- and NaCl-hematites (~3−4 × 10^{11} 1/cm^3) possessed the highest charge carrier densities among all of the tested systems. On the other hand, our charge carrier densities were all much lower than those performing high photocurrent (ca. 1.0 mA at +0.4 V vs Ag/AgCl) by approximately 9 orders of magnitude.[25] This observation highlights the important role of Sn doping in the hematite system. For example, a 0.01 atomic percent of Sn doped hematite $Fe_{1.99}Sn_{0.01}O_3$ exhibited electroconductivity of ~10^{-2} 1/(Ω cm). Such a small amount of Sn doping somehow

Table 2. Values of R^2, Slopes, and Charge Carrier Densities of Hematite Photoanodes Obtained from Various Electrolyte Solutions

anion	R^2	slope (cm^4/(F^2 V))	charge carrier density (1/cm^3)
NO_3^-	0.8732	5.96×10^{16} (1.96×10^{16})	2.96×10^{11} (9.73×10^{10})
F^-	0.6405	4.29×10^{19} (1.10×10^{19})	4.12×10^{8} (1.06×10^{8})
Cl^-	0.7326	4.99×10^{16} (1.04×10^{16})	3.54×10^{11} (7.38×10^{10})
Br^-	0.5026	7.46×10^{18} (2.62×10^{18})	2.37×10^{9} (8.32×10^{8})
I^-	0.9733	6.16×10^{18} (3.77×10^{17})	2.87×10^{9} (1.76×10^{8})

significantly increases the electroconductivity by 10 orders of magnitude of pristine (undoped) hematite Fe_2O_3 ($\sim 10^{-12}$ $1/(\Omega$ cm)).[33] Accordingly, a two-step annealing—with the first annealing at 500 °C ordering the hematite structure and the second quick annealing at 800 °C doping Sn into the hematite—is widely applied in the preparation of hematite photoanodes exhibiting high photocatalytic performance.[25,36] Given that an increased donor density decreases the thickness of the space charge layer, the higher photocurrent of the $NaNO_3$- and NaCl-hematites resulted in more-effective separation and transport of electrons and holes. In addition, relatively rodlike structures increase the electrical conductivity of hematite photoanodes. A hematite nanowire array will lead to a more-rapid collection of the majority carriers at the FTO electrode, owing to its higher electrical conductivity and fewer recombination centers at grain boundaries.[25,36]

Possible Interactions between Electrolyte Anions and Hematite during Hydrothermal Reactions. Our experiments have made it very clear that a high photoactivity is closely related to the morphology and degree of structural ordering, which further increases the conductivity and the charge carrier density. Because we annealed our samples under low temperature, we can rule out the possibility that external doping (Sn diffusion) had occurred. Accordingly, the different morphologies and degrees of structural order should reflect the history of the growth of these hematite photoanodes. Unfortunately, there are no relevant instruments that are capable of in situ probing the interaction between the electrolyte and the hematite surface during the hydrothermal reaction (120 °C in an autoclave). Recently, a series of important studies using X-ray photoelectron spectroscopy (XPS) with fast-frozen hematite colloids in aqueous solutions has shed light on the chemistry occurring at the hematite–electrolyte interface.[37−41] In those studies, hematite colloid pastes that had been equilibrated under a desired condition were fast-frozen and then introduced into the cryogenic XPS system. The photoelectron energy of the examined electrolyte ions was recorded; any energy shift could, therefore, reveal the chemical environment of these electrolyte ions. A very important interfacial phenomenon was uncovered: in an environment containing 0.05 M of a sodium halide solution, the surface loading of the halide ions decreased in the order $F^- > Cl^- \sim I^- > Br^-$, while the Na^+ loadings followed the order Na(F) > Na(I) > Na(Br) > NaCl.[37] The latter order looks like the inverse order of our photoactivity performance, NaCl ~ $NaNO_3$ > NaBr > NaI > NaF, possibly providing information regarding the hematite–electrolyte interfaces during the development of our hematite photoanodes. That is, to compensate for the elevated potentials created through surface loading of different amounts of halide anions, different amounts of Na^+ cations spontaneously accumulated at the hematite–electrolyte interfaces (Stern layer). Undoubtedly, the system will become much more complicated when the ionic strength is higher (1.0 M in our case) and some additional foreign cations (Fe^{3+} herein) are added. Literature reports have, however, suggested that increasing the ionic strength from 0.01 to 0.1 M will not influence the O-to-Fe atomic ratio significantly.[40] Thus, the degree of protonation/deprotonation is not affected by the ionic strength. On the basis of this phenomenon, a following surface complexation model, considering the capacitance of Stern layer (C_{Stern}), was proposed:

$$C_{\mathrm{Stern}} = C_{\mathrm{Stern,anion}} f_{\mathrm{anion,ads}} + C_{\mathrm{Stern,cation}} f_{\mathrm{cation,ads}}$$

where f is the fraction of adsorbed electrolyte ion. This model successfully fitted both the cation and anion surface loadings over the examined pH range and produced a value of $C_{\mathrm{Stern,Na}}$ of 3.8 F/m^2.[40] Given that $C_{\mathrm{Stern,cation}} = \varepsilon \delta_{\mathrm{cation}}{}^{-1}$, where ε is the permittivity and δ is the ionic radius, it is not difficult to imagine that, in our system, Na^+ will still be the primary cation approaching the hematite surface to compensate for the rising capacitance. Although trivalent Fe(III) cations would be more effective at compensating such an increase in potential, two factors constrain its access to the hematite surface: its smaller population (1.0 M sodium halide vs 0.1 M $FeCl_3$) and its larger ionic radius.

Because the Na^+ ion loadings followed the order Na(F) > Na(I) > Na(Br) > NaCl,[37] more Fe^{3+} cations could access the hematite surface in the NaCl solution than in the NaF solution. This concept explains why the NaCl-hematite was thicker than the other hematite photoanodes. At the same time, the higher surface coverage of Na^+ ions suppressed the NaF-hematite from developing toward the c-axis into relatively rodlike structures. Rooted on this argument, we suspect that the distinct morphologies of our hematite photoanodes arose from the different surface loading of Na^+ ions during their development stage in the hydrothermal environment. The question remains: Why were good hematite photoanodes developed only in the NaCl and $NaNO_3$ solutions? In other words, does Cl^- create a chemical environment (surface loadings and double layer thickness) similar to that of $NO_3{}^-$? To answer this question, we must consider several factors: the ion hydration radii, the surface tension of the electrolyte solution (Hofmeister series), and surface complexation modeling.

The surface loadings of both cations and anions are closely related to the water structure and the electric double layer thickness at the hematite–water interface.[37] The hydration radii of the tested ions follow the order F^- (3.52 Å) > $NO_3{}^-$ (3.35 Å) > I^- (3.31 Å) ~ Cl^- (3.32 Å) ~ Br^- (3.30 Å).[42] Because the charge-to-size ratios of $NO_3{}^-$, I^-, Cl^-, and Br^- are comparable, it appears that the ion hydration radius is not responsible for the observed phenomena. The Hofmeister series classifies ions in terms of their ability to salt out/salt in proteins; it follows the order $F^- \sim SO_4{}^{2-} > HPO_4{}^{2-} > AcO^- > Cl^- > NO_3{}^- > Br^- > ClO_3{}^- > I^- > ClO_4{}^- > SCN^-$.[43] Early members of the series increase the solvent's surface tension by strengthening the hydrophobic interactions, thereby leading to salting out of proteins (aggregate proteins). In contrast, later members lead to salting in of proteins by increasing the solubility of nonpolar molecules through a weakening of the hydrophobic effect (disperse proteins). Using the same idea when considering a colloid system, early members of the Hofmeister series help the hematite colloids aggregate into larger particles, leading to the hematite salting out from the solvent. A "salting out" chemical environment would favor the development of rodlike hematite, whereas a "salting in" environment would benefit the synthesis of hematite NPs. This Hofmeister order is in a good agreement with our observed order of photoactivity performance: NaCl- ~ $NaNO_3$- > NaBr- > NaI-hematite. It seems that the chemical environments induced by the Cl^- and $NO_3{}^-$ ions were rather comparable. Accordingly, surface tension appears to be an important factor influencing hematite development. On the basis of the Hofmeister series, it appears that the intermediate members of this series create a chemical environment that benefits the growth of hematite photoanodes; additional experiments will be necessary to quantitatively support this hypothesis. Nonetheless, it is unambiguous that the anion surface loading and, consequently, the corresponding cation loadings at the Stern layer considerably affect the growth of hematite photoanodes. Upon the basis of our results and literature reports, Figure 7 displays a possible phenomenon occurring at the hematite−electrolyte interface during the hydrothermal reaction. Specifically, an anion such as F^- that has high affinity for the surface OH groups (through the formation of hydrogen bonds) would occupy a majority of the hematite surface. This property results in a good fitting of the F^- uptake by hematite when using a thermodynamic adsorption model with consideration of inner-sphere complextion.[44] This high F^- coverage suppresses the access of Fe(III) ions and, therefore, negatively affects the hematite development. The rest of our tested anions, although they exhibit low affinity toward the hematite surface, as predicted by the Hofmeister series, provide surface loadings that directly affect the corresponding surface loadings of charge-compensating cations. From ref 37, this behavior leads to surface Na^+ loadings that follow the order Na(I) > Na(Br) > Na(Cl). Again, a high surface loading of Na^+ ions provides very limited access to the hematite surface. This phenomenon explains the lower order of the structures of the NaI- and NaBr-hematites and, therefore, why their photocatalytic performances were not comparable with those of the more highly structurally ordered NaCl- and $NaNO_3$-hematites.

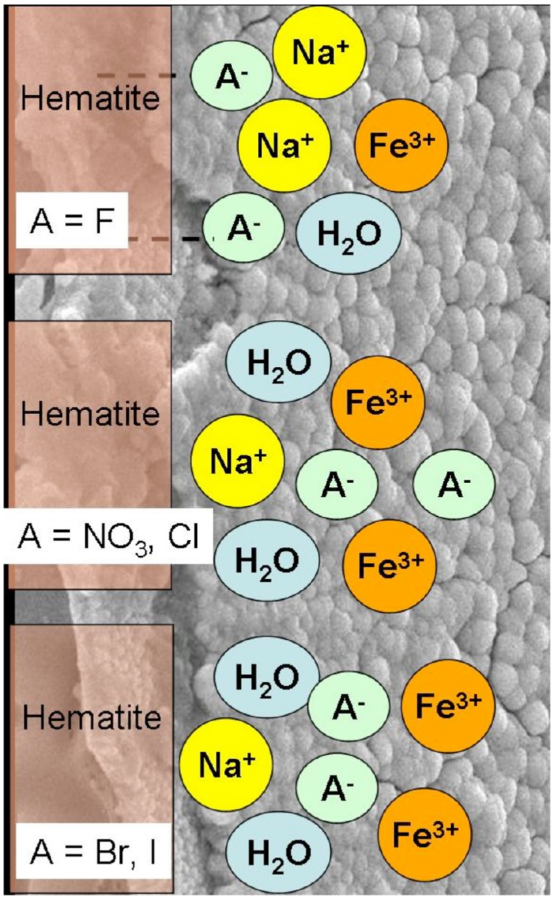

Figure 7. Proposed phenomena occurring at the hematite−electrolyte interface during hydrothermal reaction. Please refer to the text for detail descriptions of the surface loadings of Na^+ cations, water, and anions.

Despite the difficulty in acquiring relevant hematite/electrolyte interfacial phenomenon information during hydrothermal reactions (a typical XPS operation environment is below 10^{-6} Torr), we conducted a series of EIS analyses (Figure 8c) as well as LA-ICP-MS analyses (Figure 8a) instead to support our proposed interfacial phenomenon at room temperature. Further EIS measurements were conducted by placing $NaNO_3$-hematite photoanodes as working electrode in different precursor solutions (0.1 M $FeCl_3$, 1.0 M NaX, pH 1.55, Pt as counter electrode and SCE as reference electrode) to simulate the environment where these hematite photoanodes are grown. The variation of open circuit potential (OCP) of an individual system against elapsed time was first recorded (Figure 8b). EIS measurement was conducted when reaching OCP equibrium (variation <1 mV/s). In the end of each EIS measurement, individual hematite photoanode was removed from precursor solution and then dried by dipping onto tissues several times. We supposed such drying manner would remove most bulk electrolyte solution and relatively remain solution pertain to hematite/electrolyte interface. Dried hematite photoanodes were then subjected LA-ICP-MS analysis to study the surface loadings of elements including Na, N, Fe, Cl, Br, and I (Figure 8a). As indicated from Figure 8a, the intensity of Fe element remains relatively unaffected by electrolyte solution and so do Na, Cl, and N element. The relatively unaffected Fe intensity provides a basis suggesting the surface hematite coverage on each photoanode is comparable. In other words, the difference in hematite surface distribution between each photoanode sample could be reasonably negligible. On the other hand, unaffected Na intensity reflects the fact that LA-ICP-MS is not sensitive enough to distinguish a tiny difference regarding surface ion loading at a nanoscale hematite/electrolyte interface. The same argument holds for Cl and N element. Despite no significant Cl and N intensity variation was observed, clear rises of Br and I intensity are found on surface of hematite photoanode after soaking in NaBr and NaI precursor solutions. This means a significant amount of Br and I element adsorbing on surface of hematite photoanode. Such behavior did not happen on hematite surface after soaking in 1.0 M NaCl, $NaNO_3$, and NaF solutions. Our results look conflicting with those observed by Boily group, at which the surface loading of the halide ions decreased in the order $Cl^- \sim I^- > Br^-$.[37] A possible explanation could be that our solution environment is much complex than Boily group's.[37] In this study, hematite rod arrays were contacted with solutions containing 1.0 M NaX and 0.1 M $FeCl_3$ whereas in ref 37 spherelike hematite colloids were equilibrium with solutions containing solely 50 mM NaX.[37] Nonetheless, our LA-ICP-MS results clearly point out an aware amount of I^- and Br^- accumulation on hematite surface, but no significant amount of Cl^- and NO_3^- accumulation taking place at hematite surface (unfortunately, ICP-MS is not sensitive enough toward F element so that no information regarding F^- was collected).

The variation of open circuit potential (OCP) against elapsed time is shown in Figure 8b. It should be kept in mind that the variation of OCP reflects the degree of surface potential development mainly via protonation/deprotonation reaction. The E_{ocp} is rather constant in 1.0 M NaCl and NaBr solutions. In contrast, E_{ocp} gradually decreases as elapsed time in 1.0 M $NaNO_3$ and NaI solutions, while that significantly arises in 1.0 M NaF solution. It is known that a protonated (positively charged) surface often possesses a higher E_{ocp}, at which pH is lower than the pH of charge of zero potential, taking hematite for example, pH < 9.[38] In an acidic environment such as cases of those precursor solutions (pH 1.55), hematite rods are expected fully protonated ($FeOH_2^+$). From Figure 8b, equilibrated E_{ocp} values in 1.0 M $NaNO_3$, NaCl, and NaBr are rather comparable. This result is in consistent with result from Shimizu and co-workers,[37] at which zeta potentials of hematite suspension in 50 mM NaCl

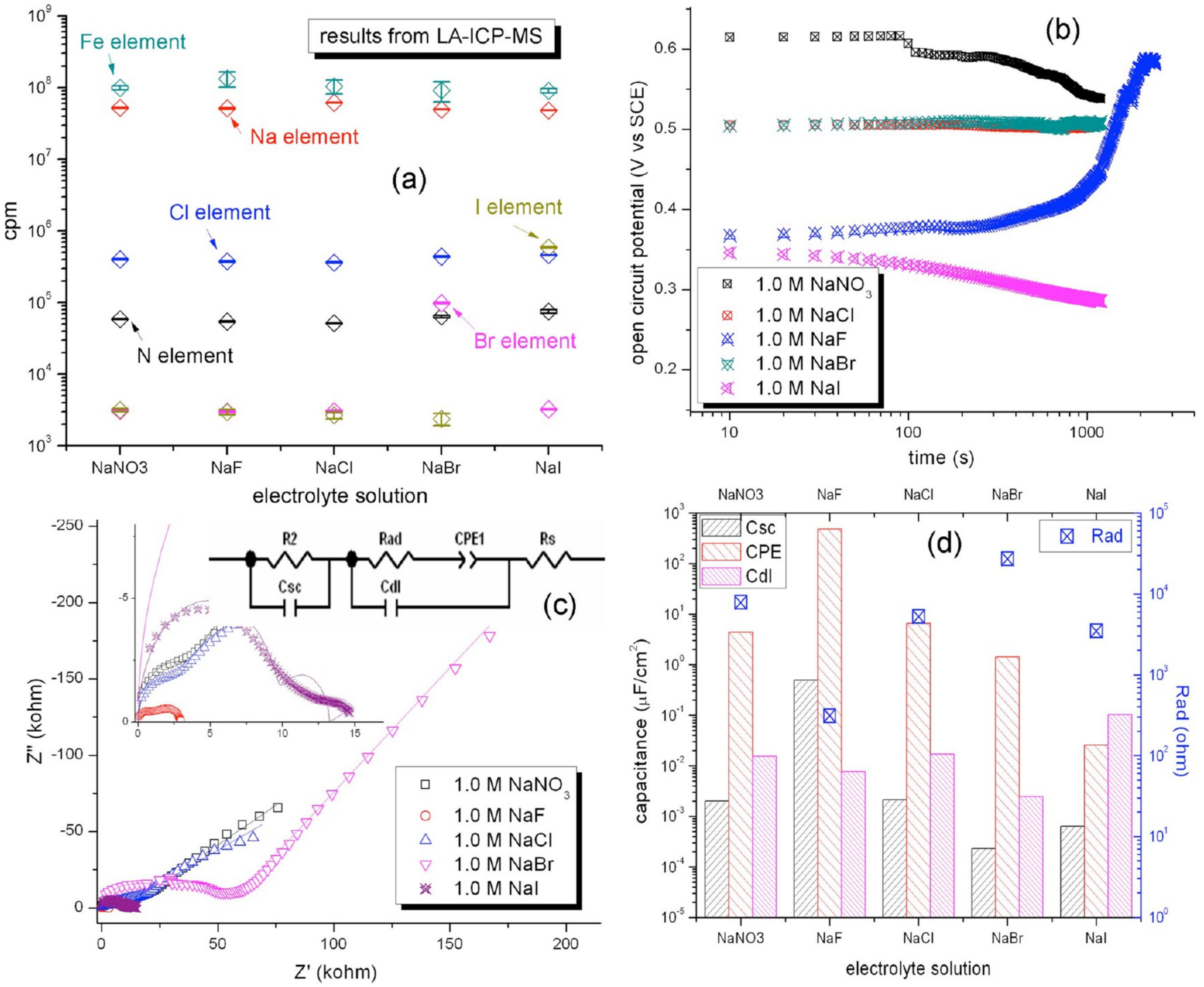

Figure 8. (a) Analyses of surface ion loadings at the hematite photoanode surface after soaking in 1.0 M $NaNO_3$, NaCl, NaF, NaBr, and NaI solutions. (b) Variation of open circuit potentials against elapsed time in solution containing 0.1 M $FeCl_3$, 1.0 M NaX, pH 1.55. (c) EIS measurements after E_{ocp} reached equilibrium with applied bias equal to corresponding equilibrated E_{ocp} values. (d) Variation of C_{sc}, CPE, C_{dl}, and R_{ad} values extracted from EIS results using equivalent circuit shown in inset of part c.

and NaBr were rather comparable. This means the degree of surface protonation of hematite in these solutions is similar. Accordingly, the cause of hematite developing toward different degree of crystallinity is the level of surface ion loadings. In other words, higher Br^- surface loading as indicated by LA-ICP-MS analysis (Figure 8a) will limit the access of Fe(III), leading hematite developing toward relatively less ordered structure. On the other hand, rising E_{ocp} in 1.0 M NaF solution suggesting an even higher degree of surface protonation. Such behavior can be rationalized by considering the (partially) hydrated F^- associated with hematite surface, which is stabilized by H—F hydrogen bonding.[37] A greater amount of F^- accumulation leads to the formation of more H—F hydrogen bonds and thus arises E_{ocp} value. In a good agreement with our proposed hematite/NaF interfacial phenomenon, a higher degree of F^- surface loading restricts the access of Fe(III) and therefore results in a relatively filmlike NaF-hematite photoanode. The gradually dropping E_{ocp} in 1.0 M NaI solution remains unclear, but a plausible explanation could be closely associated to a higher degree of I^- surface loading. Given that I^- is large and soft, unhydrated I^- in the interfacial region would somehow shield surface potential of hematite, leading to a lower E_{ocp} value.

When E_{ocp} reached equilibrium, further EIS analysis was conducted with applied bias equal to its corresponding E_{ocp} value as shown in Figure 8c. At a first glance, the impedances in NaI and NaF solutions are rather small, in comparison with those in $NaNO_3$, NaCl, and NaBr solutions. This can reflect different degrees of adsorbed ions at hematite/electrolyte interfacial region. To quantitatively interpret obtained EIS results, they were fitted by the equivalent circuit proposed by the Boily group[45] as shown in the inserted panel of Figure 8c. On the basis of a framework of equivalent circuit proposed by Boily group,[45] a Warburg element was removed since no 45° slope of impendence at high frequency region was observed. We also removed the ohmic resistance R1, which is in parallel to Warburg element, since it is difficult to extract any meaningful information from two resistances in series when only one semicircle appeared. In our reduced equivalent circuit, remained elements at solid-phase term (at hematite side) include R2 (referring to ohmic resistance + charge transfer resistance inside hematite) and C_{sc} (capacitance of space charging layer). The solution side of such interface is ascribed by R_s (solution resistance), a diffusion layer capacitance (C_{dl}), and a CPE in series of a R_{ad} (referring to resistance caused by adsorbed ions) to account for charge carrier transport from the diffusion layer to the compact layer.[45] Our best fitting results are summarized in Table 3 and Figure 8d.

Table 3. Fitting Results Based on the Hematite/Electrolyte Interface Equivalent Circuit Based on the One Proposed by the Boily Group (As Shown in the Inset of Figure 8c)[45]

element	$NaNO_3$	NaF	NaCl	NaBr	NaI
R2 (kΩ)	3.77	1.01	2.83	26.79	9.05
C_{sc} (nF/cm^2)	1.97	486.3	2.13	0.23	0.63
R_{ad} (kΩ)	7.84	0.31	5.24	27.16	3.47
CPE-T ($\mu F/cm^2$)	4.29	477	6.49	1.42	0.03
CPE-P	0.51	0.11	0.46	0.65	4.207
C_{dl} (nF/cm^2)	15.19	7.65	16.78	2.44	100.87
R_s ($\mu\Omega$)	1.03	0.62	1.03	1.03	1.20

From Table 3, the R2 value increases by roughly 10 times higher (~26 kΩ) than others when hematite photoanode is contacted with 1.0 M NaBr solution. This means surface adsorbed Br^- greatly increases the resistance of hematite. On the other hand, when hematite photoanode contacted with 1.0 M NaF solution, the C_{sc} value is about 2 orders of magnitude higher than those soaking in different sodium halide solutions. This suggests surface adsorbed F^- somehow restricts charge transfer between hematite and electrolyte, resulting in a charge accumulation at this interfacial region. Given that charge transfer at such interfacial region is mainly through the transporting of electrolyte ions toward hematite surface, a much higher C_{sc} value provides another solid evidence supporting our proposed hematite/NaF solution interfacial phenomenon (surface F^- loading hinders the access of Fe(III) from bulk electrolyte). At solution side of hematite/electrolyte interface, higher capacitances of CPE than those of C_{dl} indicate the development of compact layer in $NaNO_3$, NaCl, NaBr, and NaF solutions. The only reverse capacitance order takes place when hematite photoanode is in contact with NaI solution (CPE is 0.03 $\mu F/cm^2$ and C_{dl} is 0.10087 $\mu F/cm^2$). This is simply the result of an unusual CPE-P value of 4.027. No other good fitting results can be found when using a typical CPE value between unity and zero, meaning a more complex hematite/NaI interfacial phenomenon than our reduced equivalent circuit appears. We therefore skip further interpretation regarding the hematite/NaI interface and focus more on the comparison between each electrolyte solution. Apart from this hematite/NaI case, it is noted that the R_{ad} in the case of NaF solution (R_{ad} ~ 0.3 kΩ) is much lower than others (~5−7 kΩ in $NaNO_3$ and NaCl solution and ~27 kΩ for NaBr solution). Lower R_{ad} reflects a stronger interfacial interaction.[45] From ref 45, a considerably lower R_{ad} value of hematite contacted with 0.1 M NH_4Cl solution than with 0.1 M NaCl is ascribed to direct (hydrogen-bonded) interactions between NH_4^+ group and surface (hydro)oxo groups. We believe the same surface phenomenon taking place between F^- and hematite surface and such interaction alters the thickness of compact layer and therefore reflects in the lower R_{ad} value. A lower C_{dl} value along with a higher R_{ad} value in NaBr solution indicates a higher degree of surface complexation and a weaker interfacial interaction. The cause of such conflict behavior is unclear; however, it should be closely associated with the higher R2 as well as a lower C_{sc}. Nonetheless, it is undoubted that the consistently lower R_{ad} in cases of NaF and NaI solutions than those in $NaNO_3$ and NaCl solution indicates the interfacial interactions between NO_3^- and Cl^- and the hematite surface are weaker than those of F^- and I^- toward hematite surface. Also, higher C_{dl} in cases of $NaNO_3$ and NaCl solution than in the NaBr solution suggests a lower degree of surface complexation between NO_3^- and Cl^- and the hematite surface, which is weaker than Br^- toward the hematite surface. All of the above-mentioned hematite/electrolyte interfacial phenomena clearly evidence our proposed behavior that lower surface loadings of NO_3^- and Cl^- benefit hematite developing toward better crystallinity, a rodlike morphology, and, therefore, better photocatalytic performance. Last but not least, obtained R_s values are considerably low, reflecting the intrinsic of high conductivity in high ionic strength solutions.

CONCLUSION

In this study, we developed hematite photoanodes hydrothermally in various sodium halide solutions (NaX, X = F, Cl, Br, I) and compared their photoactivities with that of the sample obtained in $NaNO_3$ solution. Only when we used the NaCl solution did we obtain a hematite photoanode exhibiting photoactivity comparable with that of one prepared from the $NaNO_3$ solution. In contrast, the other electrolytes had a negative effect on hematite development, deteriorating the photoactivity as a result of less-ordered and filmlike structures. Consistent with previous reports, we rationalized these phenomena in terms of different degrees of anion surface loading on the growing hematites, thereby leading to different degrees of surface cation accumulation, which further influenced the access of the Fe(III) ions to the hematite surface, with a lower cation surface loading providing a favorable environment to develop a good hematite photoanode. In terms of the Hofmeister series, there appears to be a very narrow window of electrolytes that benefit the growth of hematite photoanodes, but we would require more-detailed experiments to prove it.

AUTHOR INFORMATION

Corresponding Author

*E-mail: cfwang@mx.nthu.edu.tw. Tel.: +886 (3) 573-4223. Fax: +886 (3) 572-7298.

Notes

The authors declare no competing financial interest.

ACKNOWLEDGMENTS

We thank the National Science Council (NSC102-2113-M-007-003-MY2) and Bureau of Energy, Ministry of Economy Affair, Taiwan, the Republic of China, for supporting this study. We also thank Peter Glink for his English correction.

REFERENCES

(1) Fujishima, A.; Honda, K. *Nature* **1972**, *238*, 37−38.
(2) Grätzel, M. *Nature* **2001**, *414*, 338−344.
(3) Khaselev, O.; Turner, J. A. *Science* **1998**, *280*, 425−427.
(4) Sivula, K.; Formal, F. L.; Grätzel, M. *ChemSusChem* **2011**, *4*, 432−449.
(5) Grimes, C. A.; Varghese, O. K.; Ranjan, S. Oxide Semiconducting Materials as Photoanodes. In*Light, Water, Hydrogen: The Solar Generation of Hydrogen by Water Photoelectrolysis*; Springer: Berlin, Germany, 2007; Chapter 4.
(6) Cherepy, N. J.; Liston, D. B.; Lovejoy, J. A.; Deng, H. M.; Zhang, J. Z. *J. Phys. Chem. B* **1998**, *102*, 770−776.

(7) Kennedy, J. H.; Frese, K. W. *J. Electrochem. Soc.* **1978**, *125*, 709−714.

(8) Leland, J. K.; Bard, A. J. *J. Phys. Chem.* **1987**, *91*, 5076−5083.

(9) Dareedwards, M. P.; Goodenough, J. B.; Hamnett, A.; Trevellick, P. R. *J. Chem. Soc., Faraday Trans.* **1983**, *79*, 2027−2041.

(10) Duret, A.; Gratzel, M. *J. Phys. Chem. B* **2005**, *109*, 17184−17191.

(11) Kay, A.; Cesar, I.; Gratzel, M. *J. Am. Chem. Soc.* **2006**, *128*, 15714−15721.

(12) Siula, K.; Zboril, R.; Formal, F. L.; Robert, R.; Weidenkaff, A.; Tucek, J.; Frydrych, J.; Grätzel, M. *J. Am. Chem. Soc.* **2010**, *132*, 7436−7444.

(13) Brillet, J.; Grätzel, M.; Sivula, K. *Nano Lett.* **2010**, *10*, 4155−4160.

(14) Lin, Y. J.; Zhou, S.; Sheehan, S. W.; Wang, D. W. *J. Am. Chem. Soc.* **2011**, *133*, 2398−3401.

(15) Goncalves, R. H.; Lima, B. H. R.; Leite, E. R. *J. Am. Chem. Soc.* **2011**, *133*, 6012−6019.

(16) Chen, J.; Xu, L.; Li, W. Y.; Gou, X. L. *Adv. Mater.* **2005**, *17*, 582−586.

(17) Woo, K.; Lee, H. J.; Ahn, J. P.; Park, Y. S. *Adv. Mater.* **2003**, *15*, 1761−1764.

(18) Wen, X. G.; Wang, S. H.; Ding, Y.; Wang, Z. L.; Yang, S. H. *J. Phys. Chem. B* **2005**, *109*, 215−220.

(19) Jia, C. J.; Sun, L. D.; Luo, F.; Han, X. D.; Heyderman, L. J.; Yan, Z. G.; Yan, C. H.; Zheng, K.; Zhang, Z.; Takano, M.; Hayashi, N.; Eltschka, M.; Kläui, M.; Rüdiger, U.; Kasama, T.; Gontard, L. C.; Dunin-Borkowski, R. E.; Tzvetkov, G.; Raabe, J. *J. Am. Chem. Soc.* **2008**, *130*, 16968−16977.

(20) LaTempa, J. T.; Feng, X. J.; Paulose, M.; Grimes, A. C. *J. Phys. Chem. C* **2009**, *113*, 16293−16298.

(21) Mohapatra, S. K.; John, S. E.; Banerjee, S.; Misra, M. *Chem. Mater.* **2009**, *21*, 3048−3055.

(22) Fu, Y. Y.; Wang, R. M.; Xu, J.; Chen, J.; Yan, Y.; Narlikar, A. V.; Zhang, H. *Chem. Phys. Lett.* **2003**, *379*, 373−379.

(23) Liu, J. P; Li, Y. Y; Fan, H. J.; Zhu, Z. H.; Jiang, J.; Ding, R. M.; Hu, Y. Y.; Huang, X. T. *Chem. Mater.* **2010**, *22*, 212−217.

(24) Vayssieres, L.; Beermann, N.; Lindquist, S.-E.; Hagfeldt, A. *Chem. Mater.* **2001**, *13*, 233−235.

(25) Qin, D. D.; Tao, C. L.; In, S. I.; Yang, Z. Y.; Mallouk, T. E.; Bao, N. Z.; Grimes, C. A. *Energy Fuels* **2011**, *25*, 5257−5263.

(26) Liang, X.; Wang, X.; Zhuang, J.; Chen, Y. T.; Wang, D. S.; Li, Y. D. *Adv. Funct. Mater.* **2006**, *16*, 1805−1813.

(27) Yin, W. Y.; Chen, X.; Cao, M. H.; Hu, C. W.; Wei, B. Q. *J. Phys. Chem C* **2009**, *113*, 15897−15903.

(28) Tadic, M.; Citakovic, N.; Panjan, M.; Stojanovic, Z.; Markovic, D.; Spasojevic, V. *J. Alloys Comp.* **2011**, *509*, 7639−7644.

(29) Yin, C. Y.; Minakshi, M.; Ralph, D. E.; Jiang, Z. T.; Xie, Z. H.; Guo, H. *J. Alloys Comp.* **2011**, *509*, 9821−9825.

(30) Kennedy, J. H.; Frese, K. W. *J. Electrochem. Soc.* **1978**, *125*, 709−714.

(31) Iordanova, N.; Dupuis, M.; Rosso, K. M. *J. Chem. Phys.* **2005**, *122*, No. 144305.

(32) Beermann, N.; Vayssieres, L.; Lindquist, S.-E.; Hagfeldtz, A. *J. Electrochem. Soc.* **2000**, *147*, 2456−2461.

(33) Aroutiounian, V. M.; Arakelyan, V. M.; Shahnazaryan, G. E.; Stepanyan, G. M.; Khachaturyan, E. A.; Turner, J. A. *C. R. Chimie* **2006**, *9*, 325−331.

(34) Haile, S. M.; Staneff, G.; Ryu, K. H. *J. Mater. Sci.* **2001**, *36*, 1149−1160.

(35) Lin, Y. J.; Xu, Y.; Mayer, M. T.; Simpson, Z. I.; McMahon, G.; Zhou, S.; Wang, D. W. *J. Am. Chem. Soc.* **2012**, *134*, 5508−5511.

(36) Ling, Y.; Wang, G.; Wheeler, D. A.; Zhang, J. Z.; Li, Y. *Nano Lett.* **2011**, *11*, 2119−2125.

(37) Shimizu, K.; Shchukarev, A.; Kozin, P. A.; Boily, J. F. *Langmuir* **2013**, *29*, 2623−2630.

(38) Shimizu, K.; Shchukarev, A.; Kozin, P. A.; Boily, J. F. *Surf. Sci.* **2012**, *606*, 1005−1009.

(39) Shimizu, K.; Shchukarev, A.; Boily, J. F. *J. Phys. Chem. C* **2011**, *115*, 6796−6801.

(40) Boily, J. F.; Shchukarev, A. *J. Phys. Chem. C* **2010**, *114*, 2613−2616.

(41) Shchukarev, A.; Boily, J. F.; Felmy, A. R. *J. Phys. Chem. C* **2007**, *111*, 18307−18316.

(42) Nightingale, E. R., Jr. *J. Phys. Chem.* **1959**, *63*, 1381−1387.

(43) Dos Santos, A. P.; Diehl, A.; Levin, Y. *Langmuir* **2010**, *26*, 10778−10783.

(44) Hiemstra, T.; Van Riemsdijk, W. H. *J. Colloid Interface Sci.* **2000**, *225*, 94−104.

(45) Shimizu, K.; Lasia, A.; Boily, J. F. *Langmuir* **2012**, *28*, 7914−7920.